ARTICLE

Atomic-Level Mechanistic Insights into Carbonate Electrolyte Degradation on High-Voltage $LiCoO_2$ Cathodes†

Tianxiu Yin[a,b], Junhua Jian[c], Yue Liu[a,b*], Xuewei Gu[a,b], Jinying Wu[a,b], Chao Tang[c,d*], Tao Cheng[a,b*]

a. Institute of Functional Nano & Soft Materials (FUNSOM), Jiangsu Key Laboratory for Carbon-Based Functional Materials & Devices, Joint International Research Laboratory of Carbon-Based Functional Materials and Devices, Soochow University, Suzhou 215123, China
b. Jiangsu Key Laboratory of Advanced Negative Carbon Technologies, Soochow University, Suzhou 215123, China
c. Ningde Amperex Technology Limited, Key Laboratory of Consumer Lithium-Ion Battery in Fujian, Ningde 352100, China
d. Hefei National Laboratory for Physical Science at the Microscale, CAS Key Laboratory of Materials for Energy Conversion, Department of Materials Science and Engineering, University of Science and Technology of China, Hefei 230026, China

(Dated: Received on May 21, 2025; Accepted on July 21, 2025)

Batteries power numerous technologies, yet higher energy density demands push lithium cobalt oxide ($LiCoO_2$ referred as LCO) cathodes to higher voltages, triggering unwanted chemical reactions. In this work, we investigate how carbonate-based electrolytes degrade on deeply delithiated LCO surfaces via extensive reactive molecular dynamics simulations. These simulations unveil the formation of characteristic gas products and unstable surface species, which can undermine the cathode structure and reduce battery performance. By examining different solvent compositions, the simulations reveal that partial fluorination reduces oxidative degradation and gas evolution, thus offering a route to improve interface stability. Overall, this study provides an atomic-level perspective on preventing unwanted reactions and guiding the design of safer and more robust battery systems for high-voltage applications.

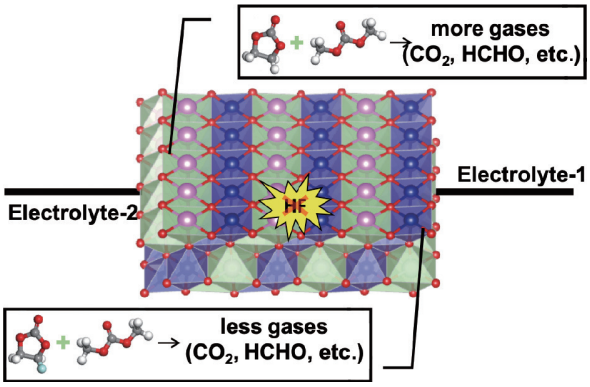

Key words: $LiCoO_2$ electrodes, Electrolyte, Reactive force field molecular dynamics, Interfacial reactions

I. INTRODUCTION

As global energy demands surge, lithium-ion batteries (LIBs) have become indispensable to both research and industrial applications. Among various cathode materials, layered lithium cobalt oxide ($LiCoO_2$), hereafter referred to as LCO, stands out for its high theoretical capacity of 274 $mA\cdot h\cdot g^{-1}$ [1], robust volumetric energy density [2], and superior lithium-ion/electron conductivity [3]. Despite these advantages, LCO cathodes typically deliver only about half of their theoretical capacity (approximately 170 $mA\cdot h\cdot g^{-1}$) because of electrolyte decomposition occurring at 4.4 V *vs.* lithium

† Part of Virtual Special Issue of "Methods, Algorithms, Codes, and Software for Theoretical and Computational Chemistry".
* Authors to whom correspondence should be addressed.
E-mail: yliu1992@suda.edu.cn, tangchao@atlbattery.com, tcheng@suda.edu.cn

(Li/Li^+) [4–6]. Extending the cutoff voltage above 4.5 V can in principle unlock additional capacity and enhance energy density. However, LCO faces severe chemical, electrochemical, structural, and thermal instabilities above 4.6 V, giving rise to phase transformations, accelerated side reactions, and persistent capacity fading [7–9].

These side reactions include the formation of a cathode electrolyte interphase (CEI), which releases gases such as O_2 and CO_2 and provokes transition metals (TMs) dissolution [10–12]. During high-voltage charging, the evolution of O_2 from LCO arises not only from lattice instability (*e.g.*, phase transitions and TM migration) but also from irreversible oxygen redox reactions, where excessive oxidation of lattice oxygen (O^{2-}) leads to oxygen release [13, 14]. A thin CEI can facilitate rapid ion transport, whereas a denser layer can mitigate TM leaching [15]. Nonetheless, dissolved TMs may diffuse to the anode, causing cross-talk effects, heightened safety concerns, and rapid capacity decline [16]. Gas evolution further complicates thermal management and may lead to catastrophic failure [17]. Although previous studies investigated gas generation and interphase composition using X-ray photoelectron spectroscopy (XPS) and pulsed electrochemical mass spectrometry (p-EC-MS), the early-stage evolution of byproducts at higher voltages remains partially understood [18].

At the atomic level, density functional theory (DFT) simulations have elucidated mechanisms such as oxidative dehydrogenation and ring-opening of carbonate solvents on LCO surfaces [19–21]. Yet, traditional DFT calculations tend to pre-assume reaction pathways, potentially overlooking the full complexity of interfacial processes. *Ab initio* molecular dynamics (AIMD) simulations capture more pathways, but they are limited by high computational costs, restricting simulation length and sometimes requiring elevated temperatures or reduced electron counts to initiate reactions [22–25]. The reactive force field (ReaxFF) approach extends both the timescale and system size, offering a more comprehensive picture of long-time scale degradation [26–28]. However, ReaxFF parameters that accurately describe LCO chemistry have been unavailable.

In this work, we build on Reddivari's [29] parameter set to develop ReaxFF parameters covering carbon (C), hydrogen (H), oxygen (O), lithium (Li), fluorine (F), phosphorus (P), and cobalt (Co) interactions. We then perform reactive molecular dynamics (RMD) simulations to probe how lithium hexafluorophosphate ($LiPF_6$) in a mixture of ethylene carbonate (EC) and dimethyl carbonate (DMC) degrades on LCO under high-voltage conditions. We validate key reaction routes using additional first-principles calculations, thereby establishing a comprehensive map of gas generation and interphase evolution. By illuminating the atomic-scale processes underlying battery failure, we aim to guide the development of safer, longer-lasting LCO-based energy storage devices.

II. COMPUTATIONAL METHODS

A. $LiCoO_2$ cathode surface models

The layered $LiCoO_2$ crystal was modeled initially in its conventional hexagonal cell ($R\bar{3}m$ space group). In this study, all simulations utilized the $Li_{0.5}CoO_2$ supercell as a model for the 4.2 V charged state, which corresponds to a delithiation level that avoids rapid capacity fading observed at higher voltages [3]. Previous studies have indicated that the (003) surface generally exhibits the highest stability, followed by the (104) surface [30]. However, the (003) surface can require specific chemical conditions to remain stable [31], so the more widely stable (104) surface was investigated here, and the simulation employed a stoichiometric slab model with a Co-O-rich terminated surface as the exposed termination facet, which can reflect the bulk properties of the material more accurately. For the DFT calculations, the $Li_{0.5}CoO_2$ (104) surface was constructed as a 1×4×4 supercell with a ~ 15 Å vacuum region along the out-of-plane (Z) direction to avoid spurious interactions between periodic images. The bottom two atomic layers were frozen to mimic the bulk environment, while the remaining layers were fully relaxed during geometry optimizations.

For the RMD simulations, the same $Li_{0.5}CoO_2$(104) surface was built as a 2×11×12 supercell to accommodate the larger simulation cell. Approximately 74 Å of electrolyte was placed atop the LCO surface at experimental concentrations. To maintain computational efficiency, the middle eight layers in the slab were held fixed, while the topmost and bottommost layers were allowed to relax during equilibration.

B. *Ab initio* calculations

All quantum-mechanical (QM) and DFT calcula-

DOI: 10.1063/1674-0068/cjcp2505068

tions were performed with the Vienna *Ab initio* Simulation Package (VASP) version 5.4.4. The projector-augmented wave (PAW) method was used for electron-ion interactions, with a plane-wave energy cutoff of 520 eV [32–34]. Spin-polarized calculations were carried out, and electron exchange-correlation effects were described using the Perdew-Burke-Ernzerhof (PBE) functional under the generalized gradient approximation (GGA) [35]. The strongly correlated d-electrons of Co were treated via DFT+U with $U=3.32$ eV [36]. Dispersion corrections were included via the DFT-D3 approach with Becke–Johnson damping [37]. For Brillouin-zone sampling, a Γ-centered Monkhorst-Pack grid of 2×3×1 was employed [38].

Ionic relaxation was carried out using the conjugate-gradient algorithm until residual forces were below 0.01 eV/Å, and electronic self-consistency was converged within 1×10^{-6} eV. The climbing image nudged elastic band (CI-NEB) method was employed to optimize the reaction pathway's minimum energy and determine the transition state structure. For equation-of-state (EOS) calculations, the plane-wave cutoff was set to 400 eV, and a self-consistent field (SCF) convergence threshold of 1×10^{-8} eV was applied. An 8×8×1 Γ-centered grid was used for accurate computations of energy band structure and density of states. The ionic relaxation threshold was 1×10^{-3} eV/Å.

C. Force field optimization

The ReaxFF parameters for C/H/O/Li/F/P/Co were optimized by matching QM data to the corresponding ReaxFF predictions (*e.g.*, bond lengths, angles, charges, and energies) [39]. The total error function in Eq.(1) sums the squared differences between QM and ReaxFF quantities (*e.g.*, bond lengths, angles, and energies), with each being scaled by weights σ_i:

$$\text{Error} = \sum_{i=1}^{n} \left(\frac{x_{i,\text{QM}} - x_{i,\text{ ReaxFF}}}{\sigma_i} \right)^2 \tag{1}$$

Monte Carlo (MC) annealing [40–42] was employed to explore the parameter space, with the acceptance probability for new parameter sets governed by:

$$P_a = \min\left\{1, \mathrm{e}^{-\beta(E_n - E_0)}\right\} \tag{2}$$

where $(E_n - E_0)$ is the difference in the objective function before and after the proposed move, $\beta=(k_\text{B}T)^{-1}$ is the reciprocal temperature factor, k_B is the Boltzmann constant, and T is the temperature. The optimization procedure was carried out using the Amsterdam Modeling Suite (AMS) 2024.102 environment [43].

D. Reactive molecular dynamics simulation

All RMD simulations were performed using the ReaxFF functional form introduced in 2008 [27] and implemented in AMS 2024.102. The simulation temperature was maintained at 298 K via the Nosé–Hoover thermostat in an NVT (constant particle number, volume, and temperature) ensemble. A damping parameter of 50 fs was used to return the system to the target temperature every 20 steps. The time step was set to 0.25 fs for stable integration.

For each simulation, a trajectory of 1.0 ns was conducted to observe electrolyte decomposition and interfacial reactivity under oxidative conditions. Beyond 1.0 ns, no further chemical reactions were detected, and the potential energy plateaued, indicating reactive equilibrium. These protocols were repeated for various electrolyte compositions (with or without fluorinated additives) to enable robust comparisons of interfacial degradation pathways.

III. RESULTS AND DISCUSSION

A. Results of the force field optimization

To enable a reactive force field framework for the LiCoO_2 cathode surface, we incorporated QM training data into the parameter-fitting process. Specifically, we extended the ReaxFF potentials to cover C, H, O, Li, F, P, Co interactions by including the results for EOS curves, bond lengths, bond angles, torsion angles, and atomic charges. FIG. 1(a) compares the ReaxFF-derived EOS curve with DFT data, showing close alignment over a broad volume range for LCO. Bulk structural properties are also captured well, as shown by the comparisons of bond lengths, bond angles, and torsion angles in FIG. 1 (c) and (d). In addition, FIG. 1(b) confirms the close match between atomic charges by ReaxFF-calculated and the Charge Model 5 (CM5) predictions. Collectively, these agreements demonstrate that the newly developed force field parameters reproduce DFT-level descriptions of LCO and form a solid basis for the large-scale RMD simulations presented below.

DOI: 10.1063/1674-0068/cjcp2505068

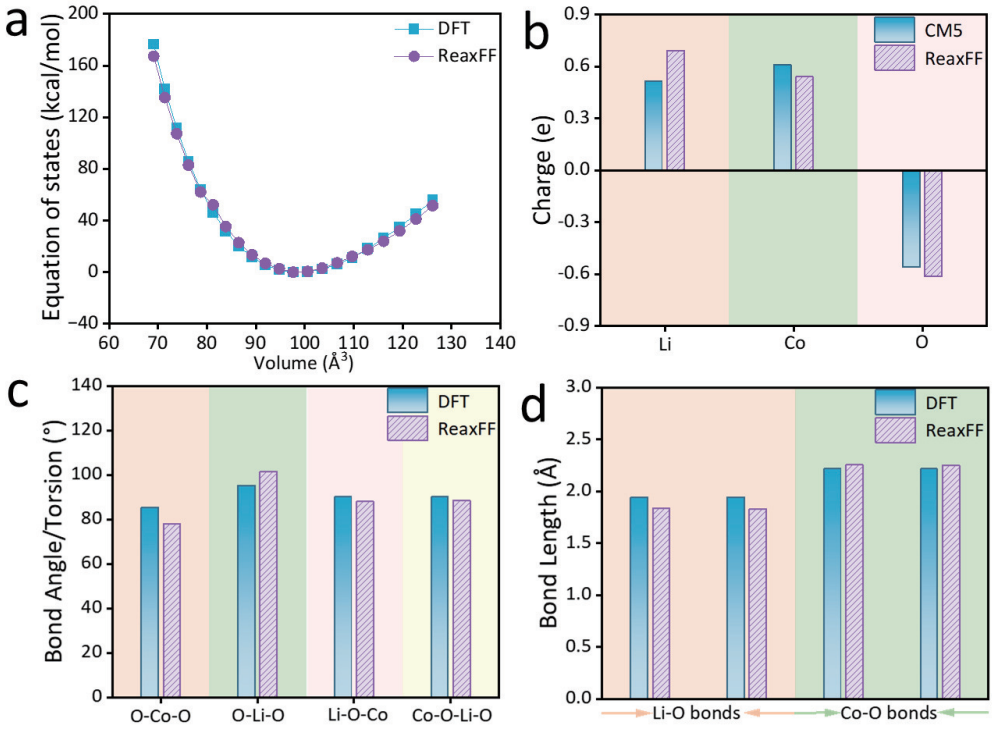

FIG. 1 Comparison of the DFT-based calculation and ReaxFF results. (a) Fitted curves of the EOS. (b) Atomic charge of $LiCoO_2$ using the CM5 and ReaxFF methods. (c) Bond angles for O–Co–O, O–Li–O, and Li–O–Co and torsion angles for Co–O–Li–O. (d) Bond length for Li–O and Co–O bonds. DFT-based results in blue and ReaxFF results in purple.

B. Degradation mechanism of electrolyte (1 mol/L $LiPF_6$ in EC/DMC (3:7, *V*/*V*)) on LCO Surfaces

A key objective of this study is to unravel the atomic-level degradation pathways of carbonate-based electrolytes on LCO surfaces, particularly under high-voltage conditions. We employed RMD simulations for 1.0 ns at 298 K to investigate the interfacial reactions between 1 mol/L $LiPF_6$ in an EC/DMC (3:7, *V*/*V*) mixture and the $Li_{0.5}CoO_2$ (104) surface. FIG. 2 (a) and (b) show initial and final atomic snapshots, indicating that reactive events occur primarily at the CEI layer.

FIG. 2 (c) and (d) illustrate how solvent molecules first adsorb onto the oxygen-rich LCO surface, leading to bond cleavage and the accumulation of decomposition products. At deep delithiation, oxygen undergoes partial oxidation, forming O_2^{n-} ($n<2$) radicals [44–46], which drive the oxidation of the electrolyte. Charge-density shifts in oxygen (FIG. 2 (e) and (f)) underscore the central role of oxygen radicals in initiating side reactions.

After 1.0 ns, both DMC and EC decompose into CO, CO_2, CH_2O, and C_2H_4 (FIG. S1 in Supplementary materials, SM), consistent with experimental observations [18, 47–49]. FIG. 3(a, b) highlight major DMC decomposition pathways initiated by C–O bond scission in the methoxy group. These processes yield intermediates such as $\cdot OCH_3$ and $CH_3O_2CO\cdot$, followed by proton-transfer reactions to form CH_2O, CH_3OH, and CO_2. FIG. 3(c) shows an alternate DMC route involving oxidative dehydrogenation before C–O bond cleavage. Meanwhile, EC predominantly undergoes ring-opening, either via direct C–O scission or oxidative dehydrogenation (FIG. 3 (d) and (e)), resulting in CO_2 along with CH_2O release [28, 50, 51].

Protons liberated at the interface can also attack PF_6^- and form hydrogen fluoride (HF) (FIG. S4 in SM), a corrosive agent that promotes LCO lattice degradation [52]. Curbing solvent dehydrogenation is therefore essential for minimizing HF formation and TM dissolution. Additional RMD simulations of pure EC and pure DMC electrolytes with $LiPF_6$ reaffirm that CO_2 is the principal byproduct from EC, whereas DMC decomposition preferentially yields methoxy species, minor CO, and CH_3OH or HCHO (FIGs. S3 and S5 in SM).

After 1.0 ns of RMD simulation, a CEI layer was formed on the surface of the LCO electrode, as illustrated in FIG. 2(d). These species exhibit low stability and heterogeneous charge distribution (FIG. S6 in SM), which may facilitate Li^+ coordination and makes them

DOI: 10.1063/1674-0068/cjcp2505068

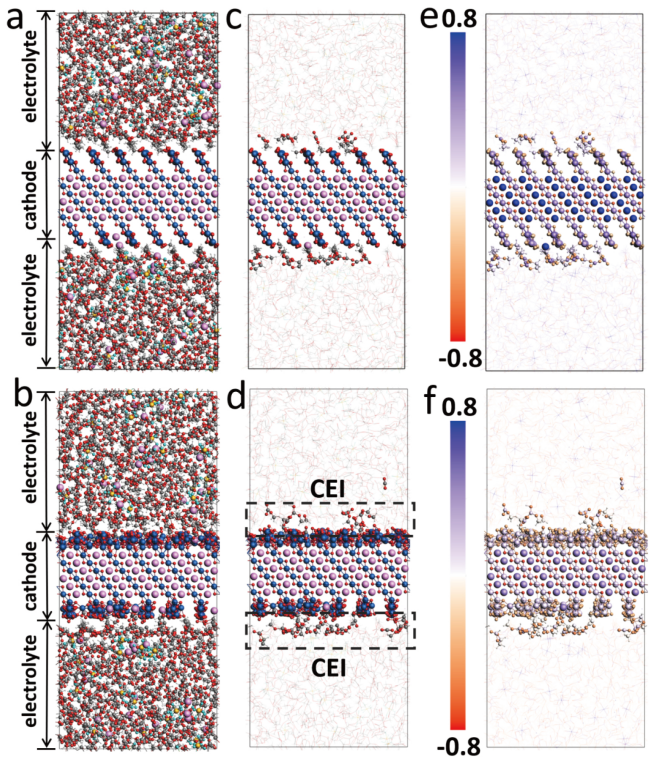

FIG. 2 Snapshots of 1 mol/L $LiPF_6$ in the EC/DMC and the cathode. (a) Initial snapshot at 0.0 ps. (b) Final snapshot at 1.0 ns. (c) Molecules involved in the reaction are highlighted in the initial snapshot at 0.0 ps. (d) Products highlighted in the final snapshot at 1.0 ns. (e) Charge distribution at 0.0 ps. (f) Charge distribution at 1.0 ns. Color codes: carbon, gray; hydrogen, white; oxygen, red; lithium, purple; fluorin, blue; phosphorus, orange; cobalt, deep blue.

prone to subsequent decomposition reactions. The organic components of the CEI primarily consist of species such as $\cdot OCO_2CH_3$ and $\cdot CH_2OCO_2CH_3$, with their specific structural formulas depicted in FIG. S1 (SM). Li *et al.* [53] conducted a detailed analysis of the formation and evolution of the CEI on layered oxide cathodes using XPS technology, revealing the presence of C–O and C=O bonds in the CEI, which aligns with the components obtained from the simulation. The formation of the inorganic component LiF in the CEI occurs through two main pathways: (1) the hydrolysis of $LiPF_6$ to generate LiF, and (2) the decomposition of the electrolyte to produce HF, which subsequently leads to the formation of LiF [54]. LiF demonstrates exceptional chemical stability, with its ionic nature establishing a uniform electrostatic field at the electrode/electrolyte interface that promotes stable Li^+ transport [55]. However, in this study, since the system simulation was conducted under dry and anhydrous conditions, $LiPF_6$ does

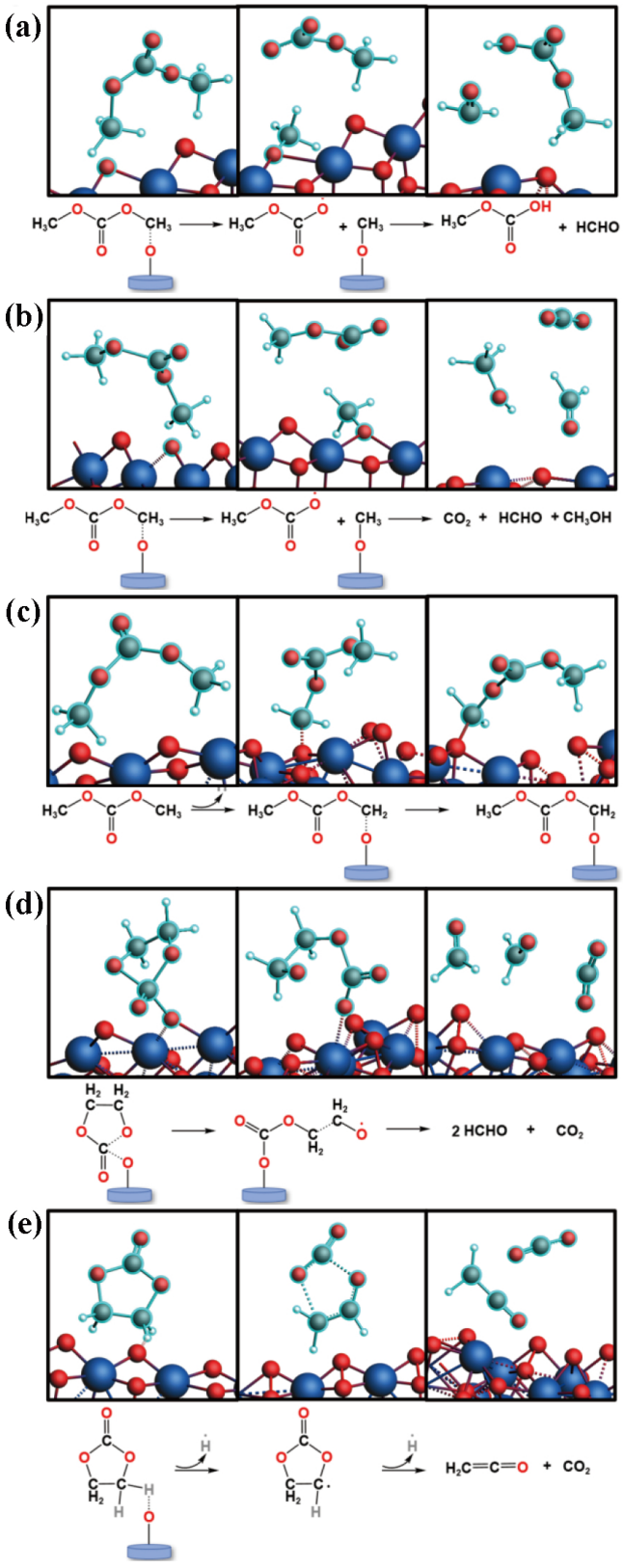

FIG. 3 DMC and EC decomposition paths for 1 mol/L $LiPF_6$ in the EC/DMC system in the RMD simulation. (a) Path 1 for DMC, (b) path 2 for DMC, (c) path 3 for DMC; (d) path 1 for EC, and (e) path 2 for EC. The color codes are the same as those in FIG. 2.

DOI: 10.1063/1674-0068/cjcp2505068

not undergo hydrolysis to form LiF. HF was observed in the pure EC and pure DMC electrolyte systems containing $LiPF_6$, suggesting that LiF molecules may form subsequently. After 1.0 ns of RMD simulation, significant amounts of CO_2 were generated from electrolyte decomposition, which may further react with H_2O and O_2 to form Li_2CO_3 [56, 57]. Taken together, these large-scale simulations confirm that: i, oxygen radicals on LCO initiate solvent oxidation; ii, ring-opening or demethylation are major routes for DMC/EC degradation; iii, proton transfer plays an important role in further byproduct formation; and iv, the formation of CEI is mainly derived from organic products formed by the oxidative decomposition of solvents.

C. DFT calculations of the decomposition of DMC and EC on the $Li_{0.5}CoO_2$(104) surface

To validate the reaction pathways suggested by RMD, we used DFT to examine four key initial decomposition steps on the $Li_{0.5}CoO_2$(104) surface. FIG. 4(a)–(d) show the structures of the optimized configuration for the reaction mechanisms. FIG. 4(e) summarize the computed Gibbs free energy (ΔG) for: (i) C–O bond cleavage in DMC, (ii) oxidative dehydrogenation of DMC, (iii) ring-opening of EC, and (iv) oxidative dehydrogenation of EC. The negative ΔG values confirm thermodynamic favorability, consistent with the RMD trajectories. These findings further validate the reliability of this force field in investigating the decomposition mechanisms of solvent molecules at the LCO interface. Specifically, C–O scission in DMC ($\Delta G \approx -1.42$ eV) is more favorable than oxidative dehydrogenation ($\Delta G \approx -0.63$ eV), mirroring the main pathways in the simulation. For EC, while ring-opening ($\Delta G \approx -1.13$ eV) and oxidative dehydrogenation ($\Delta G \approx -3.65$ eV) are both strongly exergonic, they exhibit positive activation barriers (ring-opening: 0.53 eV; oxidative dehydrogenation: 0.56 eV) (FIG. S7 in SM). This indicates that although both degradation pathways are thermodynamically favorable, the actual reactions require to overcome certain energy barriers. The relative heights of these activation barriers determine their competitive relationship under practical conditions, which collectively explains the coexistence of these two degradation mechanisms. Overall, DFT corroborates the RMD-derived picture of CO_2, radical, and intermediate formation at high voltages.

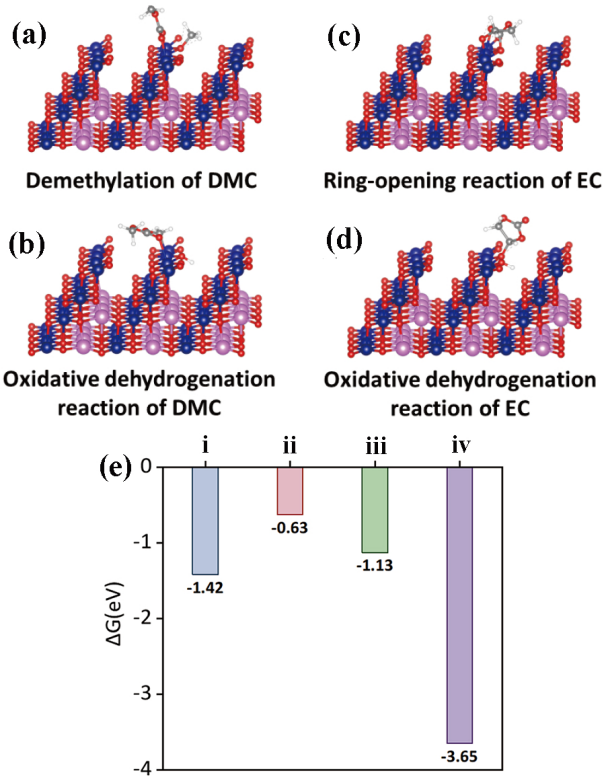

FIG. 4 The structures represent the optimized configurations for the reaction mechanisms: (a) demethylation of DMC, (b) oxidative dehydrogenation of DMC, (c) ring-opening of EC, and (d) oxidative dehydrogenation of EC. (e) ΔG of the above four response mechanisms. The color codes are the same as those in FIG. 2. i, C–O bond cleavage in DMC; ii, oxidative dehydrogenation of DMC; iii, ring-opening of EC; and iv, oxidative dehydrogenation of EC.

D. Degradation mechanism of the electrolyte (1 mol/L $LiPF_6$ in FEC/DMC (3:7, *V/V*) on LCO surfaces

Fluorinated additives, such as fluoroethylene carbonate (FEC), have been widely reported to form more robust CEIs and improve cycling stability above 4.5 V [58–60]. We replaced EC with FEC (while retaining DMC) in 1 mol/L $LiPF_6$ solutions to investigate its impact on gas evolution and side reactions. FIG. 5(d) present DFT-calculated ΔG values for FEC ring-opening and oxidative dehydrogenation. In FIG. 4(e) and FIG. 5(d), FEC shows a less exergonic pathway for hydrogen abstraction (−3.38 eV) compared with EC (−3.65 eV), implying that proton-driven reactions are somewhat suppressed.

RMD simulations (FIG. 5(e, f) and FIGs. S8, S9 in SM) confirm that FEC primarily undergoes a one-step ring-opening before stabilizing, which limits CO_2 and HCHO production. FEC can also scavenge protons at the interface and thereby reduce HF formation [22],

DOI: 10.1063/1674-0068/cjcp2505068

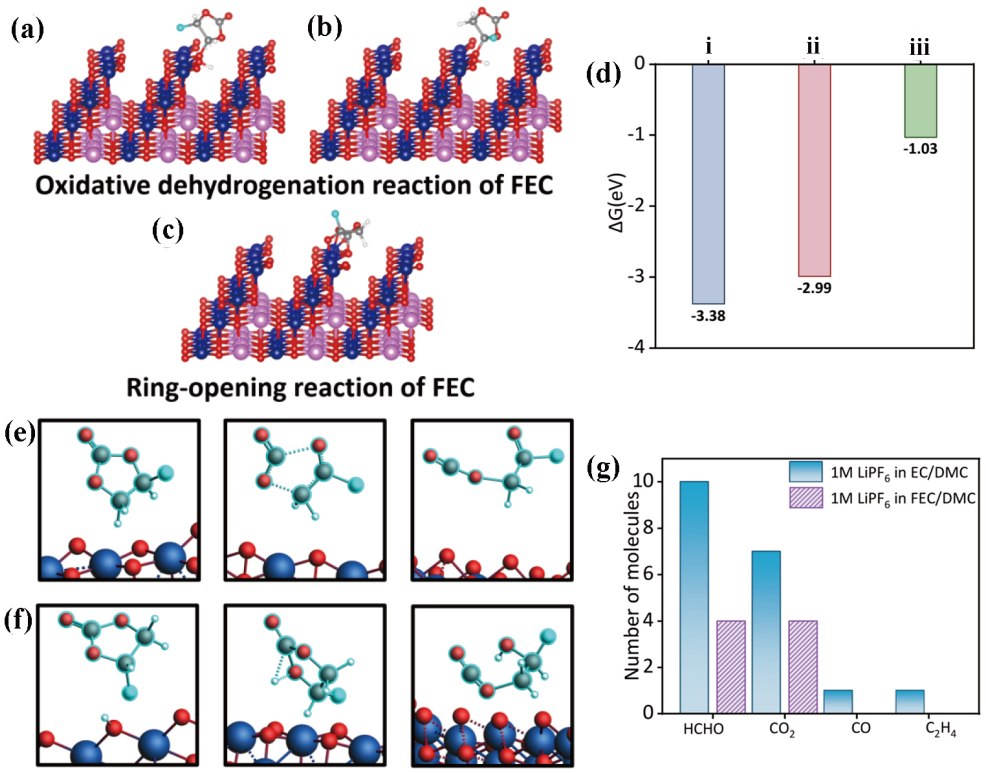

FIG. 5 The structures represent the optimized configurations for the reaction mechanisms considered: (a) oxidative dehydrogenation reaction of FEC, (b) oxidative dehydrogenation reaction of FEC (on the fluorine atom side), and (c) ring-opening reaction of FEC. (d) ΔG of the above three response mechanisms. FEC decomposition paths for 1 mol/L $LiPF_6$ in the FEC/DMC system in the RMD simulation. (e) Path 1 for FEC and (f) Path 2 for FEC. (g) Comparison of the number of final gas products between 1 mol/L $LiPF_6$ in the EC/DMC system and 1 mol/L $LiPF_6$ in the FEC/DMC system. The color codes are the same as those in FIG. 2. i, C–O bond cleavage in DMC; ii oxidative dehydrogenation of DMC; and iii, ring-opening of EC.

minimizing acid-driven lattice damage. Consequently, the total gas emission is significantly reduced compared with baseline electrolytes containing EC (FIG. 5(g)). These findings align with experiments indicating that FEC-containing electrolytes foster more stable CEIs, lessen gas evolution, and boost battery longevity. Overall, fluorinated additives help mitigate the degradation phenomena discussed in Section III.B by curbing hydrogen-driven side reactions, diminishing acid formation, and stabilizing high-voltage performance.

IV. CONCLUSION

We have developed and validated a new set of ReaxFF parameters for C/H/O/Li/F/P/Co, thus enabling large-scale investigations on LCO cathodes under high-voltage conditions. Our RMD simulations, corroborated by DFT calculations, elucidate ring-opening, demethylation, and dehydrogenation pathways that yield CO_2, CO, and other byproducts. We further show that fluorinated additives can suppress proton-driven side reactions, thereby reducing gas evolution and interphase degradation. These findings enhance our understanding of how the LCO interface deteriorates when deeply charged and outline a pathway toward more robust cathode-electrolyte systems. Future extensions may target other electrode materials and electrolyte chemistries, guiding the development of safer, longer-lasting energy storage technologies.

Supplementary materials: Computational details and the full set of developed ReaxFF parameters (C/H/O/Li/F/P/Co) are provided. FIG. S1 shows the final product distribution for 1 mol/L $LiPF_6$ in EC/DMC after 1.0 ns. Scheme S1 shows equation for DMC and EC decomposition. FIG. S2 shows detailed DMC and EC decomposition paths under RMD. FIGs. S3–S5 provide additional decomposition snapshots and paths for EC or DMC-only systems. FIG. S6 provides charge distribution of the $\cdot OCO_2CH_3$ and $\cdot CH_2OCO_2CH_3$ radicals for 1 mol/L $LiPF_6$ in EC/DMC after 1.0 ns. FIG. S7 shows the pathways for

DOI: 10.1063/1674-0068/cjcp2505068

EC dissociation on the $Li_{0.5}CoO_2$ (104) surface, with optimized reactants, products, and transition state structures. FIG. S8 provides time-evolution snapshots for 1 mol/L $LiPF_6$ in FEC/DMC, while FIG. S9 offers the final product distribution.

V. AUTHOR CONTRIBUTIONS

Tao Cheng supervised the project. Tianxiu Yin, Yue Liu, Chao Tang, and Tao Cheng conceived the idea. Tianxiu Yin, Junhua Jian and Yue Liu designed and carried out most of the calculations. Yue Liu and Tianxiu Yin performed the simulation and calculations and wrote the related sections. Tianxiu Yin, Junhua Jian and Yue Liu discussed the simulations, models, and results. Tao Cheng, Chao Tang, Yue Liu, Xuewei Gu, Jinying Wu, and Tianxiu Yin cowrote the manuscript. Tao Cheng provided fruitful suggestions. All the authors discussed the results and assisted during manuscript preparation.

VI. NOTES

The authors declare no conflicts of interest.

VII. ACKNOWLEDGMENTS

Tao Cheng acknowledges support from the National Key Research and Development Program of China (No.2022YFB2502200), and the Natural Science Foundation of Jiangsu Province (BK20230065), the Key Laboratory of Functional Nano & Soft Materials, the Collaborative Innovation Center of Suzhou Nano Science & Technology, the Priority Academic Program Development of Jiangsu Higher Education Institutions (PAPD), the 111 Project, Joint International Research Laboratory of Carbon-Based Functional Materials and Devices, Yue Liu acknowledges support from the National Natural Science Foundation of China (22303058) and the Natural Science Foundation of Jiangsu Province (BK20230475).

[1] Z. X. Wu, F. G. Zeng, H. J. Yin, L. C. Chiang, H. Q. Zhang, D. B. Zhang, K. J. Chen, W. Y. Yan, L. Y. Tang, T. H. Zhang, Y. S. Zhou, S. Q. Wang, X. X. Kuai, G. Y. Lin, L. Gu, Y. Qiao, and G. S. Sun, ACS Energy Lett. **8**, 4806 (2023).

[2] J. W. Xue, R. Gao, Z. Shi, H. X. Xiao, X. W. Zhang, R. Y. Zhang, G. Y. Zhu, I. Waluyo, Y. Li, R. M. Hill, Z. Zhu, S. Li, O. Kuznetsov, M. Y. Zhang, K. W. Lee, A. Hunt, A. Harutyunyan, Y. Shao-Horn, A. J. Johnson, and J. Li, Energy Environ. Sci. **14**, 6030 (2021).

[3] C. Y. Lyu, X. Wu, K. Wang, J. Z. Feng, T. Cheng, Y. Liu, M. Wang, M. R. Chen, M. L. Xu, J. J. Zhou, H. Y. Lu, and K. B. Guo, Adv. Energy Mater. **11**, 2000982 (2021).

[4] X. J. Zhang, F. P. Wang, X. P. Bai, L. H. Wan, F. S. Liu, S. Hou, J. X. Pu, L. J. Xia, R. W. Zhang, Y. Z. Wang, B. Nan, Y. X. Zhang, J. J. Xu, and S. C. Wang, Adv. Mater. **34**, 2108353 (2022).

[5] R. X. Yang, M. Lin, R. G. Zheng, J. Wu, S. X. Wang, C. F. Ren, G. W. Zhang, Y. Liao, M. W. Zhao, R. Z. Zhang, B. N. Xu, L. W. Yang, and Y. Yang, Adv. Funct. Mater. **30**, 2004664 (2020).

[6] Y. Y. Huang, C. Y. Zhu, Y. H. Fu, Y. M. Ou, C. C. Hu, J. S. Yu, W. Z. Hu, T. C. Chen, G. Jiang, K. H. Gu, H. Lin, W. Luo, and H. Y. Huang, Angew. Chem. Int. Ed. **60**, 4682 (2021).

[7] Y. W. Ding, Y. H. Ren, J. Z. Li, J. M. Shang, L. Y. Song, G. W. Zhao, L. Chang, L. T. Pang, Y. S. Xu, C. H. Yi, L. Zhou, H. Lin, H. Q. Zhao, and F. Pan, Adv. Energy Mater. **14**, 2303926 (2024).

[8] P. M. Wen, J. W. Kong, C. J. Zhang, H. Q. Zhang, W. Yin, N. Zhang, K. Chai, Y. Yu, C. H. Chen, and F. X. Liu, ACS Energy Lett. **7**, 4185 (2022).

[9] Y. Wang, H. Q. Zhang, C. Z. Xue, F. L. Yang, Y. J. Wang, Q. F. Meng, H. Q. Li, Y. H. Pan, N. J. Zhang, Z. Jiang, L. W. Yang, Q. X. Yu, L. Gu, and H. Li, Adv. Energy Mater. **10**, 2001413 (2020).

[10] D. L. Rinkel, P. J. Vivek, N. Garcia-Araez, and P. C. Grey, Energy Environ. Sci. **15**, 3416 (2022).

[11] J. Z. Zhang, J. Wang, Y. X. Sun, C. C. Sheng, Z. M. Cheng, H. Liu, T. Y. Wang, S. H. Zhou, and P. He, Adv. Funct. Mater. **34**, 2411409 (2024).

[12] Y. H. Yang, J. Y. Zhao, T. Qin, Y. H. Pan, H. S. Feng, Q. Li, L. X. Wang, Q. X. Yu, and H. Li, ACS Energy Lett. **9**, 4475 (2024).

[13] D. Kwon, J. S. Park, J. Lee, S. Park, H. S. Yu, and D. Kim, Adv. Sci. **10**, e2206367 (2023).

[14] J. S. Park, J. Lee, H. G. Yoon, C. Koo, H. S. Lee, S. Koo, D. Kwon, H. S. Song, Y. T. Jeon, H. Baik, H. Kim, D. Kim, and H. S. Yu, Energy Storage Mater. **53**, 340 (2022).

[15] J. Xiao, N. Adelstein, J. Y. Bi, J. W. Bian, J. Cabana, L. C. Cobb, Y. Cui, J. S. Dillon, M. M. Doeff, M. S. Islam, K. Leung, Y. M. Li, F. Lin, J. Liu, H. M. Luo, C. A. Marschilok, S. Y. Meng, Y. Qi, R. Sahore, K. G. Sprenger, C. R. Tenent, F. M. Toney, W. Tong, L. F. Wan, M. C. Wang, E. S. Weitzner, B. B. Wu, and B. Y. Xu, Nat. Energy **9**, 1463 (2024).

[16] V. Meunier, L. M. De Souza, M. Morcrette, and A. Grimaud, Joule **7**, 42 (2023).

DOI: 10.1063/1674-0068/cjcp2505068

[17] Z. Y. Song, L. Wang, L. Sheng, S. D. Ren, M. H. Liang, D. Y. Li, P. A. Wang, H. Zhang, H. Xu, and M. X. He, Energy Environ. Sci. **16**, 1943 (2023).
[18] L. Pang, R. H. Li, X. Feng, Z. W. Zhao, Y. C. Ouyang, and Q. Z. Peng, ACS Energy Lett. **9**, 3587 (2024).
[19] L. Giordano, P. Karayaylali, Y. Yu, Y. Katayama, F. Maglia, S. Lux, and Y. Shao-Horn, J. Phys. Chem. Lett. **8**, 3881 (2017).
[20] P. X. Qin, B. P. Balbuena, and H. M. Shao, J. Phys. Chem. C **123**, 14449 (2019).
[21] Y. L. Huai, L. Z. Chen, and J. Li, ACS Appl. Mater. Interfaces **9**, 36377 (2017).
[22] Y. Zheng and B. P. Balbuena, ACS Appl. Mater. Interfaces **16**, 55258 (2024).
[23] T. X. Yan, J. W. Huang, W. C. Zhu, and J. Y. Zhao, ACS Appl. Mater. Interfaces **16**, 44979 (2024).
[24] D. Zahn, J. Mol. Model **17**, 1531 (2011).
[25] Y. K. Chumbimuni-Torres, C. Thammakhet, M. Galik, P. Calvo-Marzal, J. Wu, E. Bakker, U. G. Flechsig, and J. Wang, Anal. Chem. **81**, 10290 (2009).
[26] C. T. van Duin, S. Dasgupta, F. Lorant, and A. W. Goddard, J. Phys. Chem. A **105**, 9396 (2001).
[27] K. Chenoweth, C. T. van Duin, and A. W. Goddard, J. Phys. Chem. A **112**, 1040 (2008).
[28] D. Bedrov, D. G. Smith, and C. T. van Duin, J. Phys. Chem. A **116**, 2978 (2012).
[29] S. Reddivari, C. Lastoskie, F. R. Wu, and L. J. Zhang, Front. Energy **11**, 365 (2017).
[30] Y. Kim, H. Lee, and S. Kang, J. Mater. Chem. **22**, 12874 (2012).
[31] Y. L. Hu, Z. H. Xiong, Y. C. Ouyang, Q. S. Shi, H. Y. Ji, S. M. Lei, X. Z. Wang, H. Li, J. X. Huang, and Q. L. Chen, Phys. Rev. B **71**, 125433 (2005).
[32] G. Kresse and J. Hafner, Phys. Rev. B **47**, 558 (1993).
[33] G. Kresse and J. Furthmuller, Comput. Mater. Sci. **6**, 15 (1996).
[34] G. Kresse and J. Furthmuller, Phys. Rev. B **54**, 11169 (1996).
[35] J. P. Perdew, K. Burke, and M. Ernzerhof, Phys. Rev. Lett. **77**, 3865 (1996).
[36] L. Z. Chen, J. Li, and Y. Z. Zhang, J. Mater. Chem. **22**, 18968 (2012).
[37] S. Grimme, S. Ehrlich, and L. Goerigk, J. Comput. Chem. **32**, 1456 (2011).
[38] J. H. Monkhorst and D. J. Pack, Phys. Rev. B **13**, 5188 (1976).
[39] J. Muller and B. Hartke, J. Chem. Theory Comput. **12**, 3913 (2016).
[40] A. Caflisch, P. Niederer, and M. Anliker, Proteins **14**, 102 (1992).
[41] R. S. Wilson and L. W. Cui, Biopolymers **29**, 225 (1990).
[42] R. S. Wilson, W. Cui, J. W. Moskowitz, and E. K. Schmidt, J. Comput. Chem. **12**, 342 (1991).
[43] *SCM. Amsterdam Modeling Suite (AMS), version 2024.102*, Software for Chemistry & Materials: Amsterdam, The Netherlands, (2024).
[44] T. C. Liu, L. Yu, J. J. Liu, J. Lu, X. X. Bi, A. Dai, M. Li, M. F. Li, Z. X. Hu, L. Ma, D. Luo, J. X. Zheng, T. P. Wu, Y. Ren, J. G. Wen, F. Pan, and K. Amine, Nat. Energy **6**, 277 (2021).
[45] Z. Zhu, D. W. Yu, Z. Shi, R. Gao, X. H. Xiao, I. Waluyo, M. Y. Ge, Y. H. Dong, W. J. Xue, G. Y. Xu, W. K. Lee, A. Hunt, and J. Li, Energy Environ. Sci. **13**, 1865 (2020).
[46] Z. Zhu, H. Wang, Y. Li, R. Gao, X. H. Xiao, Q. P. Yu, C. Wang, I. Waluyo, J. X. Ding, A. Hunt, and J. Li, Adv. Mater. **32**, 2005182 (2020).
[47] T. Sangsanit, K. Santiyuk, R. Songthana, K. Homlamai, S. Prempluem, W. Tejangkura, and M. Sawangphruk, J. Power Sources **611**, 234770 (2024).
[48] Y. Y. Kang, J. Wang, L. L. Du, Z. B. Liu, X. S. Zou, X. W. Tang, Z. Z. Cao, C. Y. Wang, D. J. Xiong, Q. Shi, Y. X. Qian, and Y. H. Deng, ACS Appl. Energy Mater. **2**, 8615 (2019).
[49] A. T. S. Freiberg, M. K. Roos, J. Wandt, R. de Vivie-Riedle, and H. A. Gasteiger, J. Phys. Chem. A **122**, 8828 (2018).
[50] T. Tamura, M. Kohyama, and S. Ogata, Phys. Rev. B **96**, 035107 (2017).
[51] S. Z. Xu, G. F. Luo, R. Jacobs, S. Y. Fang, M. K. Mahanthappa, R. J. Homers, and D. Morgan, ACS Appl. Mater. Interfaces **9**, 20545 (2017).
[52] J. L. Tebbe, A. M. Holder, and C. B. Musgrave, ACS Appl. Mater. Interfaces **7**, 24265 (2015).
[53] Q. H. Li, Y. Wang, X. L. Wang, X. R. Sun, J. N. Zhang, X. Q. Yu, and H. Li, ACS Appl. Mater. Interfaces **12**, 2319 (2020).
[54] Y. Zhang, Z. Z. Shen, Y. Zhang, M. Niu, L. Dong, W. P. Wang, D. X. Xu, G. Li, L. Y. Jiang, F. Wang, R. Wen, C. Yang, J. Y. Liang, S. Xin, and Y. G. Guo, Angew. Chem. Int. Ed. **64**, e202425491 (2025).
[55] H. Chen, A. Pei, D. Lin, J. Xie, A. Yang, J. Xu, K. Lin, J. Wang, H. Wang, F. Shi, D. Boyle, and Y. Cui, Adv. Energy Mater. **9**, 1900858 (2019).
[56] H. J. Guo, H. X. Wang, Y. J. Guo, G. X. Liu, J. Wan, Y. X. Song, X. A. Yang, F. F. Jia, F. Y. Wang, Y. G. Guo, R. Wen, and L. J. Wan, J. Am. Chem. Soc. **142**, 20752 (2020).
[57] G. V. Zhuang, G. Y. Chen, J. Shim, X. Y. Song, P. N. Ross, and T. J. Richardson, J. Power Sources **134**, 293 (2004).
[58] S. X. She, Y. F. Zhou, Z. J. Hong, Y. H. Huang, and Y. J. Wu, ACS Appl. Energy Mater. **6**, 7289 (2023).
[59] S. S. Yang, T. Meng, Z. C. Wang, and X. L. Hu, Energy Storage Mater. **65**, 103117 (2024).
[60] M. N. He, C. C. Su, Z. X. Feng, L. Zeng, T. P. Wu, M. J. Bedzyk, P. Fenter, Y. Wang, and Z. C. Zhang, Adv. Energy Mater. **7**, 1700109 (2017).

DOI: 10.1063/1674-0068/cjcp2505068